


Edge state in AB-stacked bilayer graphene and its correspondence with the Su-Schrieffer-Heeger ladder

Tixuan Tan¹,* Ci Li¹,† and Wang Yao^{1,2}

*Department of Physics, The University of Hong Kong, Hong Kong, China
and HKU-UCAS Joint Institute of Theoretical and Computational Physics at Hong Kong, China*

 (Received 17 September 2021; revised 5 November 2021; accepted 2 December 2021; published 20 December 2021)

We study edge states in AB-stacked bilayer graphene (BLG) ribbon where the Chern number of the corresponding two-dimensional bulk Hamiltonian is zero. The existence and topological features of edge states when two layers ended with the same or different edge terminations (zigzag, bearded, armchair) are discussed. The edge states (nondispersive bands near the Fermi level) are states localized at the edge of graphene nanoribbon that only exists in a certain range of momentum k_y . Their existence near the Fermi level are protected by the chiral symmetry with topology well described by the coupled Su-Schrieffer-Heeger (SSH) chains model, i.e., the SSH ladder, based on the bulk-edge correspondence of one-dimensional systems. These zero-energy edge states can exist in the whole k_y region when two layers have zigzag and bearded edges, respectively. A winding number calculation shows a topological phase transition between two distinct nontrivial topological phases when crossing the Dirac points. Interestingly, we find the stacking configuration of the BLG ribbon is important since it can lead to unexpected edge states without protection from the chiral symmetry both near the Fermi level in armchair-armchair case and in the gap within bulk bands that are away from Fermi level in the general case. The influence of interlayer next-nearest-neighbor interactions and interlayer bias are also discussed to fit the realistic graphene materials, which suggest the robust topological features of edge states in BLG systems.

DOI: [10.1103/PhysRevB.104.245419](https://doi.org/10.1103/PhysRevB.104.245419)

I. INTRODUCTION

One of the most attractive phenomena in condensed-matter physics is the existence and behavior of edge states, whose wave function is localized at the system's edge, of two-dimensional (2D) systems. These states are different from the bulk states in properties and play important roles in transport, e.g., quantum Hall effect (QHE) and the quantum spin Hall effect (QSHE) [1–4]. On the other hand, the existence and properties of zero-energy edge states near the Fermi level (flat bands) are usually connected with the nontrivial topological phases of the bulk system by the bulk-edge correspondence [5–9], which can be distinguished by the specific symmetry of the system and topological invariants such as the winding number [8–11].

After the progress in a decade, graphene, or the nanotube and nanoribbon, has become one of the most active two-dimensional nanomaterials in condensed-matter physics due to its excellent electrical and mechanical properties [12–20]. The free standing monolayer graphene (MLG) is a zero-gap semiconductor where the conduction and valance band touch each other at the Dirac points [19–26]. It has a trivial bulk topology as two inequivalent valleys provide opposite topological charges, leading to a zero Chern number [27]. However, edge states still exist in such graphene systems as nondispersive bands (flat bands) at the Fermi level [19,20,28–

32], which are observed by supposing a semi-infinite system, with quantized wave vectors k_y in the infinite direction [11,28,30,31,33]. The existence of these nondispersive edge states and related topology in the MLG can be further described by the bulk-edge correspondence between winding number or Zak phase of one-dimensional (1D) SSH chain systems and the existence of a localized state at the chain's edge [11,28,31,34,35], as shown in Fig. 1.

On the other hand, due to the equivalence between the graphene system and the honeycomb bosonic lattice system, i.e., the 2D magnon system which generally results from the collinear Ferromagnet after a Holstein-Primakoff transformation [36–38], edge states similar to those observed in MLG can also be found in both the related honeycomb bosonic lattices [39,40] and even nonhoneycomb bosonic lattices [41]. There are also both experimental and theoretical study on other types of edges states in photonic honeycomb lattice using different models [42,43].

In this article, we focus on the existence and topology of edge states in AB-stacked bilayer graphene (BLG) ribbon [44,45] by connecting them with k_y -parametrized SSH ladder. Earlier works are mainly concentrated on the existence of edge states of BLG under specific edge conditions [46,47] and related equivalent bilayer magnon systems [48,49], or the behavior of edge states when various symmetry-breaking terms are added [50,51]. Here the AB-stacked BLG ribbon we discuss involves three conventional edges (zigzag, bearded, and armchair, as shown in Fig. 1), whose bulk 2D system always has zero Chern number. Interlayer next-nearest-neighbor (NNN) interactions and interlayer bias are considered in terms

*ttx2000@hku.hk

†oldsmith@hku.hk

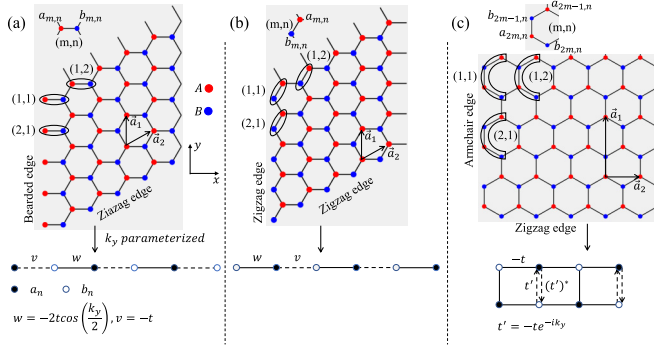


FIG. 1. The schematic illustration of nanoribbons with different edges and related effective SSH chain parametrized by k_y . The primitive vectors are \vec{a}_1 and \vec{a}_2 . The unit with translational symmetry in the tight-binding Hamiltonians is emphasized by the black box in each structure, respectively. The number pairs (1,1), (1,2), (2,1) in each figure indicate the increasing direction of m and n .

of their influence on the topology of the SSH ladder. A detailed topological classification based on discrete symmetry [10] and topological invariants calculation for effective 1D bulk Hamiltonian of SSH ladder $H(k_y, k)$ parametrized by k_y of AB-stacked BLG ribbon with various types of edge are performed, as shown in Table I. It shows the zero-energy edge states can only exist when chiral symmetry is preserved for $H(k_y, k)$ and can appear in the whole k_y region when two layers of BLG ribbon have zigzag and bearded edges, respectively. On the other hand, a straightforward calculation shows that unexpected edge states can exist in the gap within bulk bands that are away from the Fermi level. These edge states are unprotected by the chiral symmetry and are dependent on the specific edge configurations of BLG ribbon. Interlayer bias is included in our discussion because it explicitly breaks the chiral symmetry responsible for the existence of zero-energy edge states. However, edge states still exist after this chiral symmetry breaking as nonzero energy states.

TABLE I. Topological classification for different effective 1D bulk Hamiltonians $H(k_y, k)$ of a SSH chain or ladder. The related winding number W and number of zero-energy edge states N_{ES} are also shown. The topological classification is based on the presence or absence (0) of time-reversal (T), particle-hole (C), and chiral (S) symmetries [10], where all three symmetry operators are unitary, i.e., $O^\dagger O = 1$, $O = T, C, S$. They satisfy $T^\dagger H^*(k_y, k)T = H(k_y, -k)$, $C^\dagger H^*(k_y, k)C = -H(k_y, -k)$, $S^\dagger H(k_y, k)S = -H(k_y, k)$, respectively. \pm in T and C comes from $T^*T = \pm 1$ and $C^*C = \pm 1$. I_N is $N \times N$ identity matrix. $\sigma_{\alpha=x,y,z}$ represent Pauli matrices. A hyphen “-” means that there is no well-defined winding number since the chiral symmetry is broken [10]. Notice that, when an operator is written in direct product form, it can be understood as acting on different degrees of freedom (DOF). For example, $S = I_2 \otimes \sigma_z$ for $H_{\text{bea-bea}}$, where I_2 acts on layer DOF and σ_z acts on sublattice DOF.

Effective 1D bulk Hamiltonian	T	C	S	Class	W	N_{ES}
$H_{\text{bea/zig}}(k_y, k)$ [Eq. (6)]	$I_2(+)$	$\sigma_z(+)$	σ_z	\mathcal{BDI}	1,0 (Fig. 2)	2 (Fig. 2)
$H_{\text{arm}}(k_y, k)$ [Eq. (10)]	0	0	$\sigma_z \otimes \sigma_z$	\mathcal{AIII}	0 (Fig. 2)	0 (Fig. 2)
$H_{\text{arm-arm}}^\uparrow(k_y, k), U = 0$ [Eq. (14)]	0	0	$I_2 \otimes \sigma_z \otimes \sigma_z$	\mathcal{AIII}	0	0 (Fig. 4)
$H_{\text{arm-arm}}^\downarrow(k_y, k), U \neq 0$ [Eq. (14)]	0	0	0	\mathcal{A}	-	0 (Fig. 4)
$H_{\text{arm-arm}}^\uparrow(k_y, k), U = 0$ [Eq. (14)]	0	0	$I_2 \otimes \sigma_z \otimes \sigma_z$	\mathcal{AIII}	0	0 (Fig. 5)
$H_{\text{arm-arm}}^\downarrow(k_y, k), U \neq 0$ [Eq. (14)]	0	0	0	\mathcal{A}	-	4 (Fig. 5)
$H_{\text{bea-bea/zig-zig}}^\uparrow(k_y, k), U = 0$ [Eq. (16)]	$I_4(+)$	$I_2 \otimes \sigma_z(+)$	$I_2 \otimes \sigma_z$	\mathcal{BDI}	2,0 (Fig. 7)	4 (Fig. 7)
$H_{\text{bea-bea/zig-zig}}^\downarrow(k_y, k), U \neq 0$ [Eq. (16)]	$I_4(+)$	0	0	\mathcal{AI}	-	4 (Fig. 7)
$H_{\text{bea-zig}}^\uparrow(k_y, k), U = 0$ [Eq. (19)]	$I_4(+)$	$\sigma_z \otimes \sigma_z(+)$	$\sigma_z \otimes \sigma_z$	\mathcal{BDI}	-1, 1 (Fig. 7)	2 (Fig. 7)
$H_{\text{bea-zig}}^\downarrow(k_y, k), U \neq 0$ [Eq. (9)]	$I_4(+)$	0	0	\mathcal{AI}	-	2 (Fig. 7)

The rest of paper is organized as follows: We first give a brief review of the existence of edge states and the topology of MLG ribbons in Sec. II as a basis for our discussion of AB-stacked BLG ribbon. In Sec. III, we turn to the behavior and topology of edge states in AB-stacked BLG ribbons and their correspondence with the SSH ladder $H(k_y, k)$. Then we discuss the geometrical origin of the edge states appearing in the gap within bulk bands that are away from the Fermi level in Sec. IV. Finally, we present our conclusions in Sec. V as a summary.

II. EDGE STATES IN THE MONOLAYER GRAPHENE RIBBON

To discuss the existence and topological features of edge states in AB-stacked BLG ribbon, we first give a brief review of the edge states in a MLG ribbon. In general, the MLG tight-binding Hamiltonian with nearest-neighbor (NN) hopping energy t and on-site potential U_i can be written as [19]

$$H = -t \sum_{(i,j)} c_i^\dagger c_j + \sum_i U_i c_i^\dagger c_i, \quad (1)$$

where $\sum_{(i,j)}$ sums over only NN pairs. The lattice primitive vectors are \vec{a}_1 and \vec{a}_2 , which are shown in Fig. 1. As examples and without loss of generality, we mainly consider nanoribbons with three different types of edges: zigzag, bearded, and armchair in the y direction and enforce the periodic boundary condition (PBC) along this direction to see the edge states, as shown in Figs. 1(a)–(c), respectively.

A. Monolayer graphene with bearded (zigzag) edges

The tight-binding Hamiltonian of MLG with a bearded edge in the y direction, as shown in Fig. 1(a), can be expressed

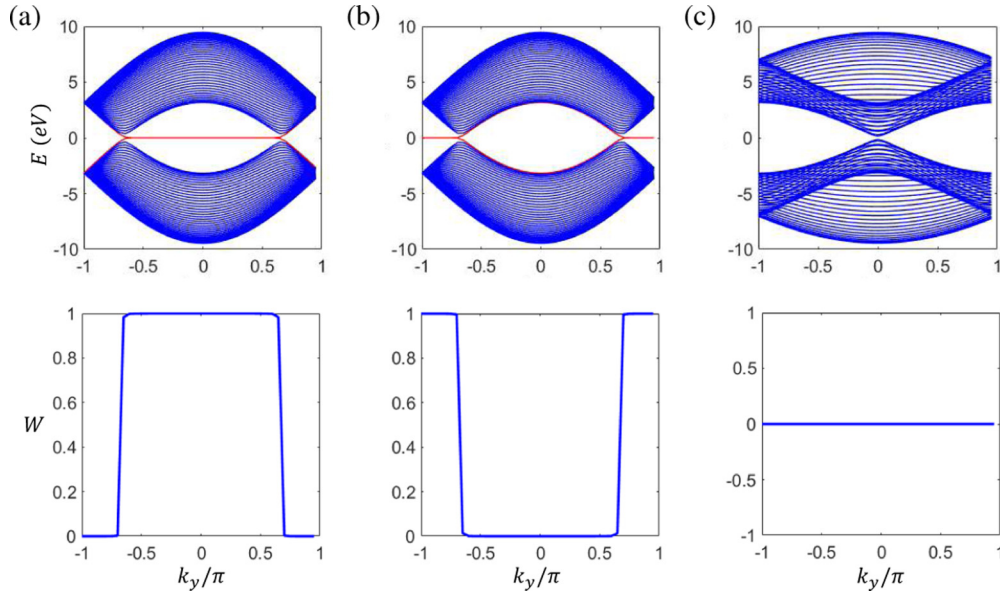


FIG. 2. The band structure of MLG ribbon and related winding number $W(k_y)$ for effective k_y -parametrized SSH chain. (a) for MLG with bearded edges, (b) for MLG with zigzag edges, and (c) for MLG with armchair edges. Here the nearest-neighbor interaction is chosen as $t = 3.16$ eV according to Ref. [52]. The red solid lines represent the edge states.

as

$$H_{\text{bea}} = -t \sum_{m=1}^M \left\{ \sum_{n=1}^N [a_{m,n}^\dagger b_{m,n} + b_{m,n}^\dagger (a_{m,n+1} + a_{m+1,n+1})] - b_{m,N}^\dagger (a_{m,1} + a_{m+1,1}) + \text{H.c.} \right\}, \quad (2)$$

where $a_{m,n}$ ($a_{m,n}^\dagger$) annihilates (creates) an electron on site (m, n) on sublattice A (an equivalent definition is used for sublattice B). The system is assumed infinite along the m direction and finite along the n direction. The minus term in the curly brackets gives the open boundary condition (OBC) in the finite direction. The Fourier transformation along the infinite direction is

$$f_{m,n} = \frac{1}{\sqrt{M}} \sum_{k_y} e^{ik_y m} f_{k_y,n}, \quad f = a, b, \\ k_y = \frac{2\pi(m - M/2)}{M}, \quad m = 0, 1, 2, \dots, M-1, \quad (3)$$

and leads to

$$H_{\text{bea}}(k_y) = -t \left\{ \sum_{n=1}^{N-1} [a_{k_y,n}^\dagger b_{k_y,n} + (1 + e^{ik_y}) b_{k_y,n}^\dagger a_{k_y,n+1}] + a_{k_y,N}^\dagger b_{k_y,N} + \text{H.c.} \right\}, \quad (4)$$

which is equivalent to an effective SSH chain parametrized by k_y as below. Notice that we have made a redefinition of basis by a phase such that the hopping becomes real and it is easier to make an association with the original SSH chain model. Not doing such a redefinition would leave the coupling complex,

but all results in this paper are not affected:

$$H_{\text{bea}}(k_y) \simeq \sum_{n=1}^{N-1} (v a_n^\dagger b_n + w b_n^\dagger a_{n+1}) + v a_N^\dagger b_N + \text{H.c.}, \\ w = -2t \cos \frac{k_y}{2}, \quad v = -t. \quad (5)$$

The bulk Hamiltonian of this equivalent chain is

$$H_{\text{bea}}(k_y, k) = \eta^\dagger h_b(k_y, k) \eta, \quad \eta = (a_k, b_k)^T, \\ h_b(k_y, k) = \begin{bmatrix} 0 & v + w e^{-ik} \\ v + w e^{ik} & 0 \end{bmatrix}, \quad (6)$$

which belongs to the nontrivial topological class \mathcal{BDI} (see Table I for details).

We plot the band structure of bearded-edge graphene nanoribbon and winding number for the bulk Hamiltonian $H_{\text{bea}}(k_y, k)$ (6) as a function of parameter k_y in Fig. 2(a), respectively. The winding number we used in this paper is defined as [10]

$$W = -\frac{i}{4\pi} \int_{\text{BZ}} dk \text{Tr}(S Q^{-1} \partial_k Q), \quad (7)$$

with

$$Q(k) = I_N - 2\mathcal{P}(k), \quad \mathcal{P}(k) = \sum_{\alpha < 0} |u_\alpha\rangle \langle u_\alpha|. \quad (8)$$

$\alpha < 0$ refers to the occupied bands [eigenstates of $H(k_y, k)$ below the Fermi level]. $Q^{-1}(k) = Q(k)$, as $Q^2 = I_N$. Winding number describes the topological properties near the zero energy (Fermi level) of 1D bulk Hamiltonians $H(k_y, k)$ with the chiral symmetry operator S [10]. Here we would like to stress again that one should not confuse k_y with k , since k_y appearing in the bulk Hamiltonian $H(k_y, k)$ is a parameter of the system and k is the wave vector of the effective SSH chain when its length is taken to be infinite. The integration appearing

in the definition of W is over k , with W being a function of k_y . A concrete example with some details omitted here is given in the Appendix to make clearer the origin of k_y and k . The zero-energy edge states (flat bands) exist in the restricted region $k_y \in [-\pi, -\frac{2}{3}\pi] \cup [\frac{2}{3}\pi, \pi]$ and correspond to $W = 1$, which agrees with previous literature [27,31]. The effective 1D Hamiltonian $H_{\text{zig}}(k_y)$ for MLG with a zigzag edge can be obtained by switching w and v , a_n and b_n in $H_{\text{bea}}(k_y)$ as the zigzag edge is related with the bearded edge through an exchange of basis and coupling [see Figs. 1(a) and 1(b)]. In terms of their corresponding SSH chain, zigzag nanoribbons and bearded nanoribbons differ from each other by a switch between intercell coupling and intracell coupling of the chain. It can be observed from Figs. 2(a) and 2(b) that zero-energy edge states (flat bands) of $H_{\text{zig}}(k_y)$ and nonzero winding number of $H_{\text{zig}}(k_y, k)$ appear in regions of k_y complementary to the one with bearded edges.

B. Monolayer graphene with armchair edges

The tight-binding Hamiltonian of a MLG ribbon with an armchair edge is different from the previous case, which is

$$\begin{aligned} H_{\text{arm}} = & -t \sum_{n=1}^N \left[\sum_{m=1}^{M/2} (a_{2m,n}^\dagger b_{2m,n} + b_{2m,n}^\dagger a_{2m,n+1}) \right. \\ & + a_{2m-1,n}^\dagger b_{2m-1,n} + b_{2m-1,n+1}^\dagger a_{2m-1,n} \\ & \left. + \sum_{m=1}^M a_{m+1,n}^\dagger b_{m,n} \right] \\ & + \sum_{m=1}^{M/2} t (b_{2m,N}^\dagger a_{2m,1} + b_{2m-1,1}^\dagger a_{2m-1,N}) + \text{H.c.}, \quad (9) \end{aligned}$$

where $M/2 \in \mathbb{N}$. Unit with translational symmetry of this ribbon in Fig. 1(c) is constructed as $(m, n) \simeq (b_{2m-1,n}, a_{2m-1,n}, a_{2m,n}, b_{2m,n})$. The effective Hamiltonian parametrized by k_y for this ribbon is no longer a single SSH chain but two coupled uniform chains, as shown in Fig. 1(c). The coupled chains have the bulk Hamiltonian:

$$\begin{aligned} H_{\text{arm}}(k_y, k) = & \eta^\dagger h_a(k_y, k) \eta, \quad \eta = (b_k^1, a_k^1, a_k^2, b_k^2)^T, \\ h_a(k_y, k) = & -t \begin{bmatrix} h(k) & D(k_y) \\ D^*(k_y) & h(k) \end{bmatrix}, \\ h(k) = & \begin{bmatrix} 0 & 1 + e^{-ik} \\ 1 + e^{ik} & 0 \end{bmatrix}, \\ D(k_y) = & \begin{bmatrix} 1 & 0 \\ 0 & e^{-ik_y} \end{bmatrix}, \quad (10) \end{aligned}$$

where the superscript 1/2 distinguishes even and odd since there are two sets of A and B in each unit of armchair MLG shown in Fig. 1(c):

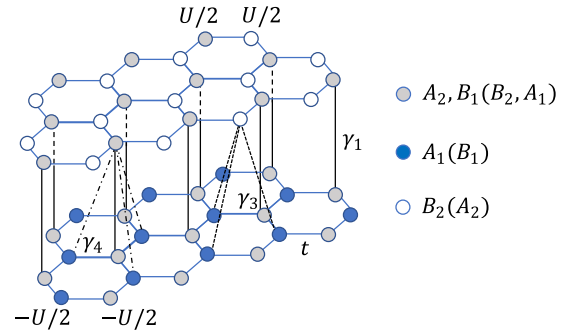


FIG. 3. The atomic structure of AB-stacked BLG in side view.

$$\begin{aligned} f_k^1 = & \frac{1}{\sqrt{N}} \frac{1}{\sqrt{M/2}} \sum_{j=1}^{M/2} \sum_{n=1}^N e^{-ikn} e^{-ik_y j} f_{2j-1,n}, \\ f_k^2 = & \frac{1}{\sqrt{N}} \frac{1}{\sqrt{M/2}} \sum_{j=1}^{M/2} \sum_{n=1}^N e^{-ikn} e^{-ik_y j} f_{2j,n}. \quad (11) \end{aligned}$$

$f = a, b$ as shown in Fig. 1. Notice again that k is the wave vector of the coupled chains while k_y is a parameter of its coupling. This bulk Hamiltonian of the coupled chains belongs to the nontrivial topological class \mathcal{AIII} (see Table I for details). Here we would like to point out that, although it belongs to the nontrivial topological class, the winding number is zero in the whole region of k_y and there are no edge states, as shown in Fig. 2(c), which means this is a trivial case.

III. EDGE STATES NEAR THE ZERO ENERGY (FERMI LEVEL) IN THE AB-STACKED BILAYER GRAPHENE

Based on the three different graphene nanoribbons discussed in the last section, there are four types of AB-stacked BLG ribbons, i.e., arm-arm (both layers are armchair edges), zig-zig/bea-bea (both layers are zigzag or bearded edges), and bea-zig (one layer is bearded edges and the other is zigzag edges), as listed in Table I. They can be summarized by the tight-binding Hamiltonian [19,45,53]

$$H = \sum_l H_{\text{edge}}^l + H_{\text{int}} + H_{\text{on-site}}, \quad (12)$$

where $l = 1, 2$ are labels of the bottom and top layers, respectively. $H_{\text{on-site}}$ refers to the on-site energy of carbon atoms such as interlayer bias U as shown in Fig. 3. It includes contributions from both layers. H_{int} describes the van der Waals interaction between two layers [19,45,53]. The meanings of various interlayer couplings γ_i with $i = 1, 3, 4$ are indicated in Fig. 3. Here, we take $t = 3.16$ eV, $\gamma_1 = 0.381$ eV as typical experimental values for AB-stacked BLGs [52], and $\gamma_4 = 0$ throughout this work since it is pretty small compared with others in realistic systems [19,52,53]. We choose $\gamma_3 = 0.38$ eV $\approx \gamma_1$ when considering nonzero γ_3 , which is close to most of the experimental observations [19,52,53].

A. AB-stacked bilayer graphene with armchair-armchair edges

Next we discuss these four types of AB-stacked BLG structures in detail. To form an AB-stacked BLG ribbon, armchair

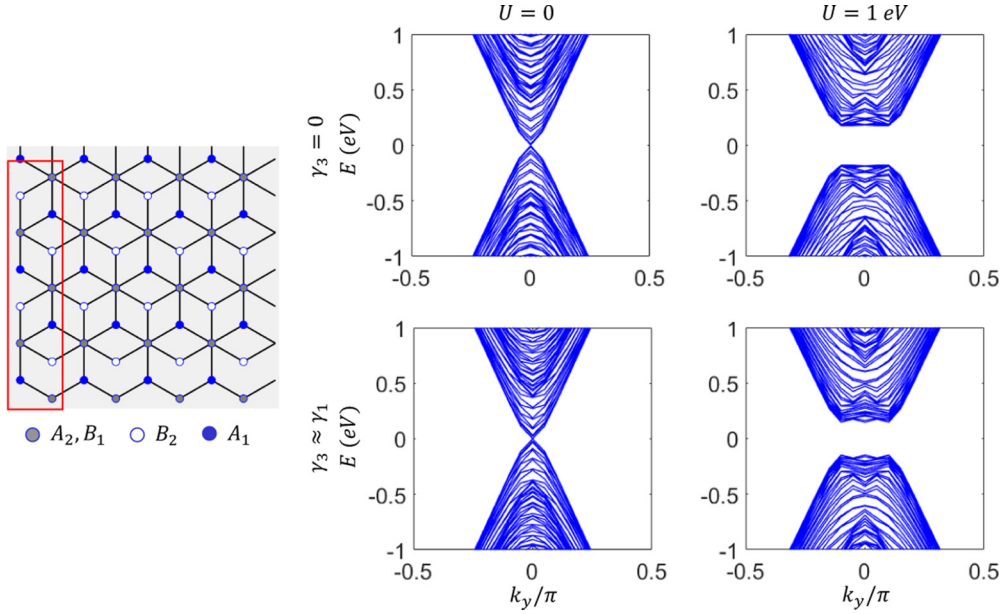


FIG. 4. (left panel) The atomic structure of an armchair-armchair AB-stacked BLG ribbon in top view, corresponding to the 1D effective Hamiltonian $H_{\text{arm-arm}}^{\uparrow}(k_y, k)$ [Eq. (14)]. The edge configuration is emphasized by the red box. (right panel) Related band structure with different interlayer bias U and NNN interaction γ_3 .

MLG can only be stacked with the other armchair MLG, but not with zigzag/bearded MLG (see Fig. 1). Thus, we first consider the Hamiltonian

$$H_{\text{arm-arm}} = \sum_l H_{\text{arm}}^l + H_{\text{int}} + H_{\text{on-site}}, \quad (13)$$

where both layers have armchair edge. We further consider two different edge configurations as shown in the left panel

of Figs. 4 and 5, corresponding to different H_{int} . The band structure of $H_{\text{arm-arm}}^{\uparrow(\downarrow)}(k_y)$ parametrized by k_y is shown in the right panel of Figs. 4 and 5 respectively, where the label \uparrow (\downarrow) represents the different edge configuration of the two settings. It denotes the direction to translate the top layer if we effectively consider that the AB-stacked nanoribbon is formed from the relative translation between two layers of AA-stacked nanoribbon. Similar calculation to that of last

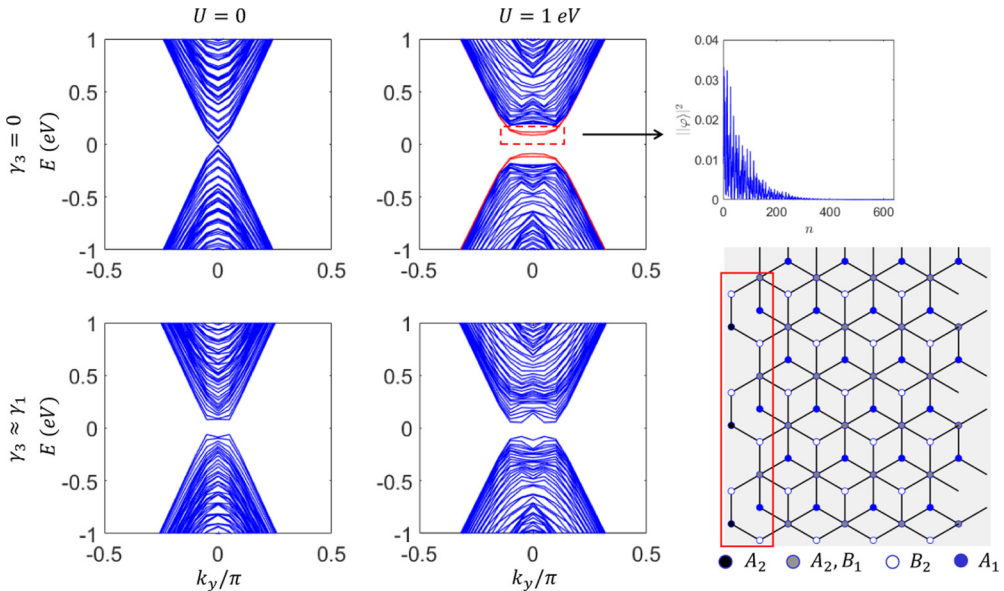


FIG. 5. (right panel) The atomic structure of an armchair-armchair AB-stacked BLG ribbon in top view, corresponding to the 1D effective Hamiltonian $H_{\text{arm-arm}}^{\downarrow}(k_y, k)$ [Eq. (14)]. The edge configuration is emphasized by the red box, which is different from the one in Fig. 4. (left panel) Related band structure with different interlayer bias U and NNN interaction γ_3 . The red solid lines are the edge states. There are four of them. The wave function distribution in real space of a typical edge state in the red dashed box is shown on the right side. The vertical axis is the wave function's amplitude, and the horizontal axis is the site index, which increases along the finite direction of the ribbon.

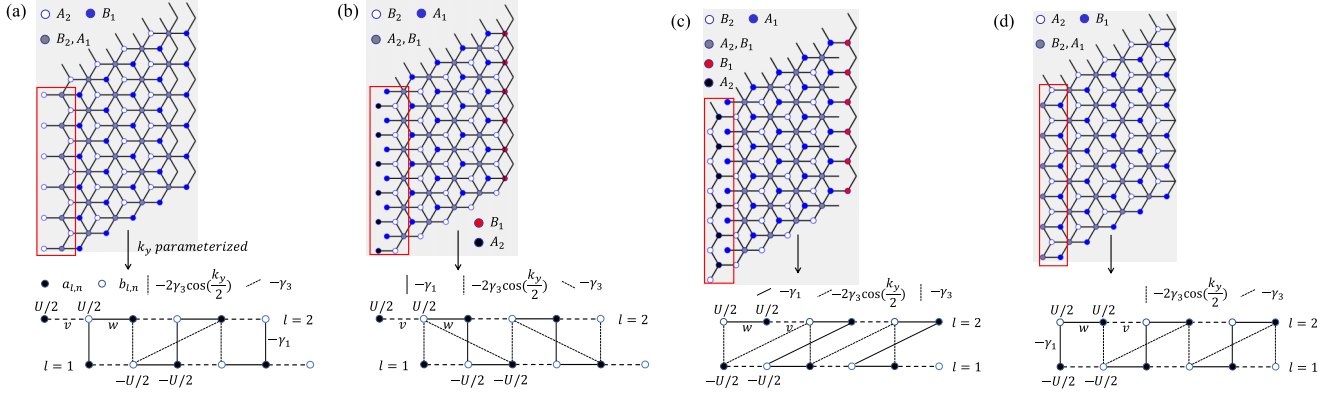


FIG. 6. The atomic structure of (a), (b) bearded-bearded and (c), (d) bearded-zigzag AB-stacked BLG ribbon in top view. The specific edge configuration is emphasized by the red box. The related k_y -parametrized SSH ladders are shown at the bottom, where panels (a) and (b) corresponds to $H_{\text{ber-ber}}^{\leftarrow(\swarrow)}(k_y, k)$ [Eq. (16)] and panels (c) and (d) corresponds to $H_{\text{ber-zig}}^{\leftarrow(\swarrow)}(k_y, k)$ [Eq. (19)], respectively. $w = -2t \cos(k_y/2)$ and $v = -t$ are the same as used in Fig. 1.

section shows that the related k_y -parametrized bulk Hamiltonian is

$$\begin{aligned}
 H_{\text{arm-arm}}^{\uparrow(\swarrow)}(k_y, k) &= \eta^\dagger h_{\text{aa}}^{\uparrow(\swarrow)}(k_y, k) \eta, \quad \eta = (\xi_1, \xi_2)^T, \\
 \xi_l &= (b_{l,k}^1, a_{l,k}^1, a_{l,k}^2, b_{l,k}^2), \\
 h_{\text{aa}}^{\uparrow(\swarrow)}(k_y, k) &= \begin{bmatrix} h_a^{\uparrow(\swarrow)}(k_y, k) & -H_{\text{int}}^{\uparrow(\swarrow)}(k_y, k) \\ -[H_{\text{int}}^{\uparrow(\swarrow)}(k_y, k)]^\dagger & h_a^{\downarrow(\swarrow)}(k_y, k) \end{bmatrix}, \\
 h_a^{\uparrow(\swarrow)}(k_y, k) &= \frac{(-1)^l U}{2} I_4 + h_a(k_y, k), \quad f_k = 1 + e^{ik}, \\
 H_{\text{int}}^{\uparrow(\swarrow)}(k_y, k) &= \begin{bmatrix} 0 & 0 & \gamma_1 & 0 \\ \gamma_3 f_k & 0 & 0 & \gamma_3 \\ \gamma_3 e^{ik_y} & 0 & 0 & \gamma_3 f_k^* \\ 0 & \gamma_1 e^{ik_y} & 0 & 0 \end{bmatrix}, \\
 H_{\text{int}}^{\leftarrow(\swarrow)}(k_y, k) &= \begin{bmatrix} 0 & \gamma_1 & 0 & 0 \\ \gamma_3 e^{ik} & 0 & 0 & \gamma_3 f_k e^{-ik_y} \\ \gamma_3 f_k & 0 & 0 & \gamma_3 \\ 0 & 0 & \gamma_1 e^{ik} & 0 \end{bmatrix}, \quad (14)
 \end{aligned}$$

which belongs to the nontrivial topological class \mathcal{AIII} when there is no interlayer bias. When $U \neq 0$, it belongs to the trivial topological class \mathcal{A} (Table I).

For the BLG ribbon with the edge configuration shown in Fig. 4, there is no edge state even if nonzero U and γ_3 are considered. For the other edge configuration as shown in Fig. 5, the edge states which are gapped and flat appear when nonzero interlayer bias is added. Here we would like to point out that these edge states are not topological for three reasons: (i) They cannot be described by the bulk-edge correspondence we used before since their energy is not at the Fermi level. (ii) They are not robust since they disappear when including γ_3 , the quantity that preserves the original chiral symmetry of the system, and do not influence the existence of edge states in the case of bilayer bearded-bearded (zigzag-zigzag) ribbon (discussed below). (iii) Most importantly, they are not formed between two Dirac points with different topological charges [27,30,31,54] in the band structure. But this fact is still interesting since it indicates that the existence of edge states can be determined by interlayer bias.

B. AB-stacked bilayer graphene with bearded-bearded (zigzag-zigzag) edges

The Hamiltonian for which both layers have a bearded edge is analogous to the one with a zigzag edge. We take the one with the bearded edge as an example, whose Hamiltonian can be expressed as

$$H_{\text{bea-bea}} = \sum_l H_{\text{bea}}^l + H_{\text{int}} + H_{\text{on-site}}. \quad (15)$$

There are two different edge configurations, corresponding to different forms of H_{int} . Here these two types of Hamiltonians are denoted $H_{\text{bea-bea}}^{\leftarrow}(k_y)$ and $H_{\text{bea-bea}}^{\leftarrow(\swarrow)}(k_y)$. The corresponding lattice structures are shown in Figs. 6(a) and 6(b), respectively. Meanwhile, $H_{\text{zig-zig}}^{\leftarrow}(k_y)$ and $H_{\text{zig-zig}}^{\leftarrow(\swarrow)}(k_y)$ are obtained by the substitutions $w \leftrightarrow v$, $a_{l,n} \leftrightarrow b_{l,n}$ in Figs. 6(a) and 6(b). The bulk Hamiltonian of the k_y -parametrized SSH ladder $H_{\text{bea-bea}}^{\leftarrow}(k_y)$ and $H_{\text{bea-bea}}^{\leftarrow(\swarrow)}(k_y)$ can be expressed as

$$\begin{aligned}
 H_{\text{bea-bea}}^{\leftarrow(\swarrow)}(k_y, k) &= \eta^\dagger h_{\text{bb}}^{\leftarrow(\swarrow)}(k_y, k) \eta, \\
 \eta &= (a_{1,k}, b_{1,k}, a_{2,k}, b_{2,k})^T, \\
 h_{\text{bb}}^{\leftarrow(\swarrow)}(k_y, k) &= \begin{bmatrix} h_b^{\leftarrow(\swarrow)}(k_y, k) & H_{\text{int}}^{\leftarrow(\swarrow)}(k_y, k) \\ [H_{\text{int}}^{\leftarrow(\swarrow)}(k_y, k)]^\dagger & h_b^{\leftarrow}(k_y, k) \end{bmatrix}, \quad (16)
 \end{aligned}$$

with

$$h_b^{\leftarrow(\swarrow)}(k_y, k) = h_b(k_y, k) + \frac{(-1)^l}{2} U I_2, \quad l = 1, 2, \quad (17)$$

$$\begin{aligned}
 H_{\text{int}}^{\leftarrow}(k_y, k) &= - \begin{bmatrix} 0 & \gamma_1 \\ \gamma_3 e^{ik} (2 \cos \frac{k_y}{2} + e^{ik}) & 0 \end{bmatrix}, \\
 H_{\text{int}}^{\leftarrow(\swarrow)}(k_y, k) &= - \begin{bmatrix} 0 & \gamma_3 (2 \cos \frac{k_y}{2} + e^{-ik}) \\ \gamma_1 e^{ik} & 0 \end{bmatrix}.
 \end{aligned}$$

which belongs to nontrivial class \mathcal{BDI} only when $U = 0$, otherwise it belongs to trivial class \mathcal{AI} (Table I).

Unlike the armchair-armchair-edge case, the different geometry (distinguished by arrows) of bearded-bearded

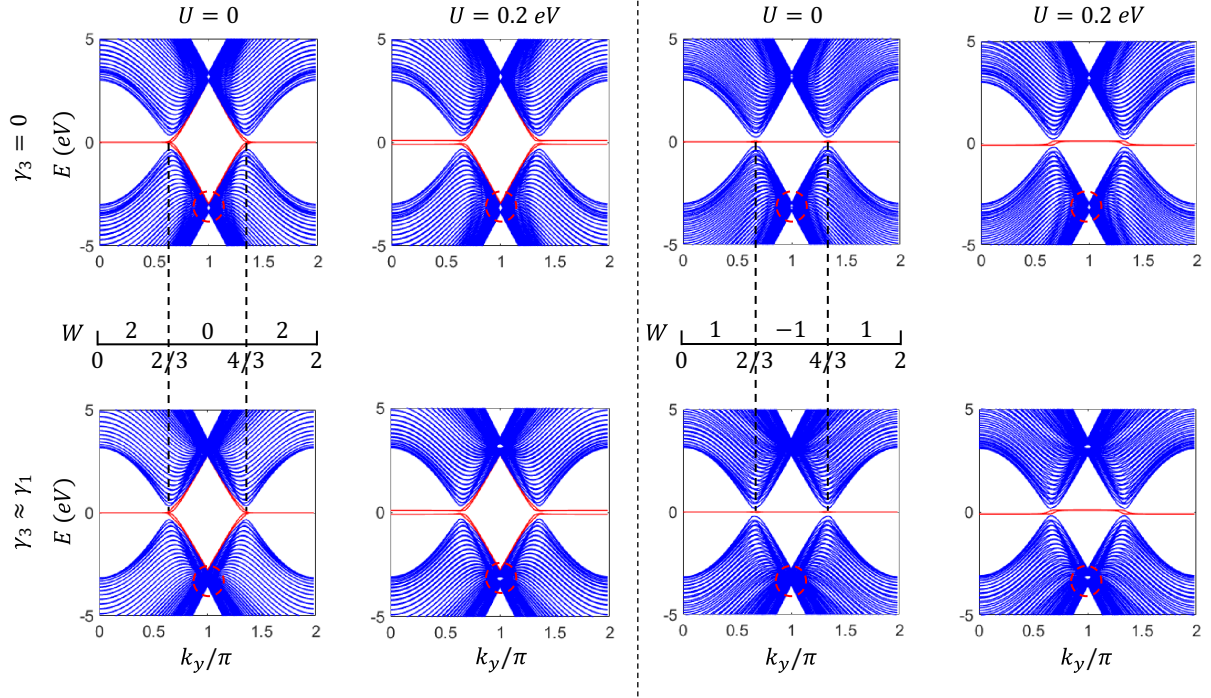


FIG. 7. (left panel) Band structure with different interlayer bias U and NNN interaction γ_3 corresponding to the atomic structure shown in Fig. 6(a). (right panel) Band structure with different interlayer bias U and NNN interaction γ_3 corresponding to atomic structure shown in Fig. 6(d). The red solid lines show the edge states. Related winding number $W(k_y)$ is shown in the middle for $U = 0$ cases in both panels, where the chiral symmetry is preserved. The red dashed circle marks the energy band area within bulk bands where the unexpected edge states may appear, which is discussed in detail in Fig. 9.

(zigzag-zigzag) edges of BLGs do not influence the band structure and edge states near the zero-energy (Fermi level). So we only show the band structure of bearded-bearded nanoribbon corresponding to $H_{\text{bea-bea}}^{\leftarrow}(k_y)$ in the left panel of Fig. 7 for simplicity. The nontrivial and trivial topological classification straightly determines the existence of zero-energy edge states since U breaks the chiral symmetry. The zero-energy edge states appear as flat fourfold degenerate bands when $U = 0$, belonging to nontrivial topological class. The related winding number calculation tells that they correspond to a winding number $W = 2$ when they are flat and $W = 0$ when they enter the bulk bands. Flat bands from each layer are separated by a gap when $U \neq 0$, as shown in Fig. 7. Bulk Hamiltonian of the SSH ladder $H_{\text{bea-bea}}(k_y, k)$ ($U \neq 0$) belongs to topological trivial class (Table I). Here the edge states for $U \neq 0$ are still topological since they connect two topologically different Dirac points [54].

C. AB-stacked bilayer graphene with bearded-zigzag edges

Armchair MLG ribbon can only be stacked with armchair MLG ribbon to form an AB-stacked BLG ribbon. In contrast, zigzag MLG ribbon can be stacked with bearded MLG ribbon to form an AB-stacked BLG ribbon, which is described by the Hamiltonian

$$H_{\text{bea-zig(zig-bea)}} = H_{\text{bea(zig)}}^1 + H_{\text{zig(bea)}}^2 + H_{\text{int}} + H_{\text{on-site}}, \quad (18)$$

Here we choose $H_{\text{bea-zig}}$ as an example. The situation is the same as what we found in above section, where different edge

configurations lead to similar band structures and related edge states near the zero energy. Hamiltonians of different edge configurations can be denoted as $H_{\text{bea-zig}}^{\leftarrow}(k_y)$ or $H_{\text{bea-zig}}^{\rightarrow}(k_y)$ as shown in Figs. 6(c) and 6(d), respectively. The bulk Hamiltonian of the SSH ladder $H_{\text{bea-zig}}^{\leftarrow}(k_y)$ or $H_{\text{bea-zig}}^{\rightarrow}(k_y)$ can be expressed as

$$H_{\text{bea-zig}}^{\leftarrow(\rightarrow)}(k_y, k) = \eta^\dagger h_{\text{bz}}^{\leftarrow(\rightarrow)}(k_y, k) \eta, \\ \eta = (a_{1,k}, b_{1,k}, b_{2,k}, a_{2,k})^T, \\ h_{\text{bz}}^{\leftarrow(\rightarrow)}(k_y, k) = \begin{bmatrix} h_{\text{b}}^1(k_y, k) & H_{\text{int}}^{\leftarrow(\rightarrow)}(k_y) \\ [H_{\text{int}}^{\leftarrow(\rightarrow)}(k_y)]^\dagger & h_{\text{z}}^2(k_y, k) \end{bmatrix}, \quad (19)$$

with

$$h_{\text{b}}^1(k_y, k) = h_{\text{b}}(k_y, k) - \frac{U}{2} I_2, \\ h_{\text{z}}^2(k_y, k) = h_{\text{z}}(k_y, k) + \frac{U}{2} I_2, \\ H_{\text{int}}^{\leftarrow}(k_y) = - \begin{bmatrix} \gamma_3 (2e^{ik} \cos \frac{k_y}{2} + 1) & 0 \\ 0 & \gamma_1 e^{ik} \end{bmatrix}, \\ H_{\text{int}}^{\rightarrow}(k_y) = - \begin{bmatrix} \gamma_1 & 0 \\ 0 & \gamma_3 (2 \cos \frac{k_y}{2} + e^{ik}) \end{bmatrix}. \quad (20)$$

When $U = 0$, $H_{\text{bea-zig}}^{\leftarrow}(k_y)$ belongs to the nontrivial class \mathcal{BDI} . Otherwise, it belongs to the trivial class \mathcal{AI} (Table I). The band structure of nanoribbon corresponding to $H_{\text{bea-zig}}^{\leftarrow}(k_y)$ is plotted in right panel of Fig. 7. The twofold degenerate

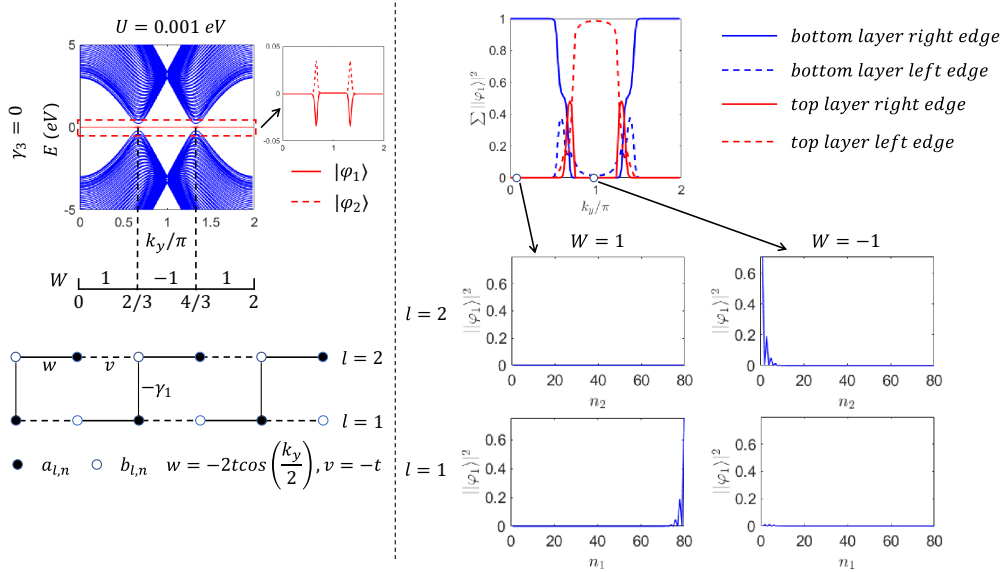


FIG. 8. (left panel) Band structure with interlayer bias $U \approx 0$ and zero NNN interaction γ_3 . Corresponding SSH ladder parametrized by k_y is shown at the bottom. The reason for using $U \approx 0$ is explained in the text. (right panel) The distribution of the wave function $|\varphi_1\rangle$ on different edges and different layers as a function of k_y and the distribution of the wave function $|\varphi_1\rangle$ in real space for two typical k_y values with two different winding numbers. $n_{l=1,2}$ is a site index on the respective layer, which increases along the finite direction of the ribbon. A transition between bottom-left and top-right is observed when crossing the Dirac point.

zero-energy edge state (flat band) can exist in the whole k_y region when $U = 0$. It corresponds to a topological phase transition between two nontrivial topological phases characterized by $W = -1$ and $W = 1$ when crossing the Dirac point, as shown in the left panel in Fig. 7. When $U \neq 0$, although the chiral symmetry is broken (i.e., no well-defined winding number), the topological edge state still exists in the whole k_y region with different energies when crossing the Dirac point. Notice that, when $U \neq 0$, the bands are no longer twofold degenerate, as explained later.

This topological phase transition is not a numerical artifact. In contrast, it is protected by interlayer coupling. Winding number describes the mapping of Brillouin zone (k) to $U(n)$ group, whose fundamental group is Z [55]. In the BLG ribbon case, it is $U(2)$. This mapping is orientation sensitive. For example, in calculating the winding number of BLG bea-bea ribbon, as presented in Fig. 7. The nonzero winding number of it can be turned into -2 instead of 2 by reversing the direction of k . In the BLG bea-zig case, as in the right panels of Fig. 7, it is the bearded layer or zigzag layer that is responsible for the 1 or -1 part of winding number. If we can choose the orientation of k independently for each layer, we can make the winding number always 1 , i.e., no phase transition is present. This simple conjecture can be verified by setting $\gamma_3 = \gamma_1 = 0$, i.e., two decoupled ribbons. In that case, one can indeed find a chiral operator S such that the calculated winding number is always 1 (or always -1). For example, it can be done by using $S = \text{diag}(1, -1, 1, -1)$ for the Hamiltonian in Eq. (19) with $\gamma_3 = \gamma_1 = 0$. It is permissible for an uncoupled system to have different orientation of Brillouin zone for each subsystem. However, the presence of interlayer coupling, which is present in the real BLG ribbon system, prohibits us from choosing the orientation of k independently for each layer. We are forced to choose the same orientation

of k for two layers of ribbon. Otherwise, we are not able to write H_{int} in Bloch form. More specifically, this means that $S = \text{diag}(1, -1, 1, -1)$ is no longer a chiral symmetry operator for Eq. (19) with nonzero interlayer coupling. In this sense, the observed topological phase transition is protected by interlayer coupling.

The change in winding number can be seen from the behavior of the wave function of edge states. For the region $W = 1$ ($|v| < |w|$), one of the degenerate edge states can be approximately expressed as

$$|\varphi_1\rangle \approx \frac{1}{\sqrt{\Omega_1}} \sum_{j=1}^N \left(-\frac{v}{w}\right)^{N-j} b_{1,j}^\dagger |0\rangle, \quad \Omega_1 = \frac{1 - (v/w)^{2N}}{1 - (v/w)^2} \approx \frac{w^2}{w^2 - v^2}, \quad (21)$$

for $\gamma_3 = U \approx 0$, which is equivalent to one of the edge states of MLG ribbon with bearded edges (bottom layer), as shown in Fig. 8, where the label $l = 1$ (2) in $a_{l,j}^\dagger$ ($b_{l,j}^\dagger$) represents the bottom (top) layer. The other edge state is

$$|\varphi_2\rangle \approx \frac{1}{\sqrt{\Omega_2}} \sum_{j=1}^N \left[\left(-\frac{v}{w}\right)^{j-1} a_{1,j}^\dagger |0\rangle + (-1)^j j \frac{\gamma_1}{w} \left(\frac{v}{w}\right)^{j-1} a_{2,j}^\dagger |0\rangle \right], \quad \Omega_2 = \frac{1 - (v/w)^{2N}}{1 - (v/w)^2} + \left(\frac{\gamma_1}{w}\right)^2 \sum_{j=1}^N j^2 \left(\frac{v}{w}\right)^{2j-2} \approx \frac{w^2}{w^2 - v^2} + \left(\frac{\gamma_1}{w}\right)^2 \sum_{j=1}^N j^2 \left(\frac{v}{w}\right)^{2j-2}. \quad (22)$$

Since $\gamma_1 \ll t$ (one order smaller in our choice of parameters), $|\varphi_2\rangle$ mainly distributes on the $l = 1$ layer. When entering the $W = -1$ ($|v| > |w|$) region, $|\varphi_1\rangle$ and $|\varphi_2\rangle$ continuously change to

$$\begin{aligned} |\varphi_1\rangle &\rightarrow \frac{1}{\sqrt{\Omega_1}} \sum_{j=1}^N \left[\left(-\frac{w}{v}\right)^{j-1} b_{2,j}^\dagger |0\rangle \right. \\ &\quad \left. + (-1)^j j \frac{\gamma_1}{v} \left(\frac{w}{v}\right)^{j-1} b_{1,j}^\dagger |0\rangle \right], \\ \Omega_1 &= \frac{1 - (w/v)^{2N}}{1 - (w/v)^2} + \left(\frac{\gamma_1}{v}\right)^2 \sum_{j=1}^N j^2 \left(\frac{w}{v}\right)^{2j-2} \\ &\approx \frac{v^2}{v^2 - w^2} + \left(\frac{\gamma_1}{v}\right)^2 \sum_{j=1}^N j^2 \left(\frac{w}{v}\right)^{2j-2}, \end{aligned} \quad (23)$$

and

$$\begin{aligned} |\varphi_2\rangle &\rightarrow \frac{1}{\sqrt{\Omega_2}} \sum_{j=1}^N \left(-\frac{w}{v}\right)^{N-j} a_{2,j}^\dagger |0\rangle, \\ \Omega_2 &\approx \frac{v^2}{v^2 - w^2}. \end{aligned} \quad (24)$$

This indicates that when the winding number changes, the distribution of edge states in real space will switch both edge and layer, as shown in Fig. 8.

We would like to stress that when U is exactly zero, one can argue that $|\varphi_1\rangle$ and $|\varphi_2\rangle$ are exponentially degenerate. The degeneracy originates from the edge degree of freedom. Thus, any linear combination of them are still edge states, with $|\varphi_1\rangle$ and $|\varphi_2\rangle$ being only one possible choice. Then it does not make sense to discuss the behavior of $|\varphi_1\rangle$ in real space when crossing the Dirac point, e.g., from bottom-left to top-right, as a linear combination would mix the left edge and right edge. The naturalness of choosing $|\varphi_1\rangle$ and $|\varphi_2\rangle$ is seen as follows: when a small positive bias U , e.g., 0.001 eV, is included as perturbation H_{per} , the cross term $\langle \varphi_1 | H_{\text{per}} | \varphi_2 \rangle = 0$. According to the first-order degenerate perturbation theory [56], $|\varphi_1\rangle$ and $|\varphi_2\rangle$ are the good states to use in perturbation. The energy of the state in Eq. (22) would increase relatively to the energy of the state in Eq. (21) because the former has a minor component on the $l = 2$ layer. Similarly, the energy of the state in Eq. (24) would increase relatively to the energy of the state in Eq. (23) because the latter has minor component on the $l = 1$ layer. Thus, $|\varphi_1\rangle/|\varphi_2\rangle$ would continuously evolve into Eq. (23) or Eq. (24). Figure 8 is plotted with $U = 0.001$ eV and $\gamma_3 = 0$. The behavior of states is numerically smooth, indicating that the degeneracy is effectively lifted with a small bias.

IV. EDGE STATES APPEARING IN THE GAP AWAY FROM THE ZERO ENERGY (FERMI LEVEL)

In the above sections, we have considered two edge configurations of BLG bea-zig ribbon and two edge configurations of BLG bea-bea ribbon, denoted via different arrows. It was shown that, for example, two edge configurations of BLG bea-bea ribbon have the same topology. It turns out that the difference between these two edge configurations appears in the form of nontopological edge states, as discussed below.

Besides the topological edge states we discussed in the last section, which exist as gapless or gapped flat bands near the zero energy (Fermi level), some unexpected edge states are found in the gap within bulk bands that are away from the zero energy (Fermi level) in the AB-stacked BLGs with a bearded-bearded (zigzag-zigzag) edge or a bearded-zigzag edge, as shown in Fig. 9. The existence and number of these edge states are determined by the specific edge configurations of AB-stacked BLGs. These unexpected edge states appear in the region near $k_y = \pi$ in all situations, which reminds us that their appearance may be relevant to the effective Hamiltonians $H(k_y = \pi)$ for different types of edge configurations.

Therefore, we show the lattice structure of the effective Hamiltonians $H(k_y = \pi)$ for different types of edge configurations in Fig. 10, where some couplings vanish since $\cos(\pi/2) = 0$. $H_{\text{bea-bea}}^{\leftarrow}(k_y = \pi)$ with $\gamma_3 = 0$ describes the simply repeated decoupled four-site structures

$$\begin{aligned} h_4 &= w_{eq} c_1^\dagger c_2 + v_{eq} c_2^\dagger c_3 + w_{eq} c_3^\dagger c_4 \\ &+ \text{H.c.} + \sum_{j=1}^2 \frac{(-1)^{j+1} U}{2} (c_{2j-1}^\dagger c_{2j-1} + c_{2j}^\dagger c_{2j}), \end{aligned} \quad (25)$$

as shown in Fig. 10(a). Each four-site structure would provide four energy levels

$$\begin{aligned} E &= \pm \frac{1}{2} \sqrt{2\gamma_1^2 + U^2 + 4t^2} \pm 2\varepsilon, \\ \varepsilon &= \sqrt{4U^2 t^2 + 4t^2 \gamma_1^2 + \gamma_1^4}, \end{aligned} \quad (26)$$

and each of these four energy levels are highly degenerate since there are many identical four-site structures. When we consider the region close to $k_y = \pi$, each of the four highly degenerate levels would split into many bulk states according to first-order degenerate perturbation theory. So there are no edge states under this scenario in the neighborhood of $k_y = \pi$ in the bulk gap.

If $\gamma_3 \approx \gamma_1$ as discussed before, the energy bands of $H_{\text{bea-bea}}^{\leftarrow}(k_y = \pi)$ is dominated by not only a simply repeated decoupled four-site structure but also a newly formed SSH chain:

$$\begin{aligned} h_{\text{SSH}} &= \sum_{n=1}^N w_{eq} a_n^\dagger b_n + v_{eq} b_n^\dagger a_{n+1} + \text{H.c.} \\ &+ \sum_{n=1}^N \frac{(-1)^{n+1} U}{2} (a_n^\dagger a_n + b_n^\dagger b_n), \end{aligned} \quad (27)$$

as shown in Fig. 10(a). Because $t \gg \gamma_1$ in our choice of parameters [52], which is general in most cases [19,53], this equivalent SSH chain leads to no edge states. This is in accord with the results shown in both Figs. 7 and 9(a).

However, the situation is different for $H_{\text{bea-bea}}^{\leftarrow}(k_y)$. When $\gamma_3 = 0$, two isolated two-site structures,

$$h_2 = w_{eq} c_1^\dagger c_2 + \text{H.c.} \pm \frac{U}{2} (c_1^\dagger c_1 + c_2^\dagger c_2), \quad (28)$$

appear in addition to repeated decoupled four-site structures, as shown in Fig. 10(b). These isolated two-site structures provide the eigenstates with energy $\pm U/2 \pm t$, as shown in Fig. 9(b). When we consider the region close to $k_y = \pi$, since

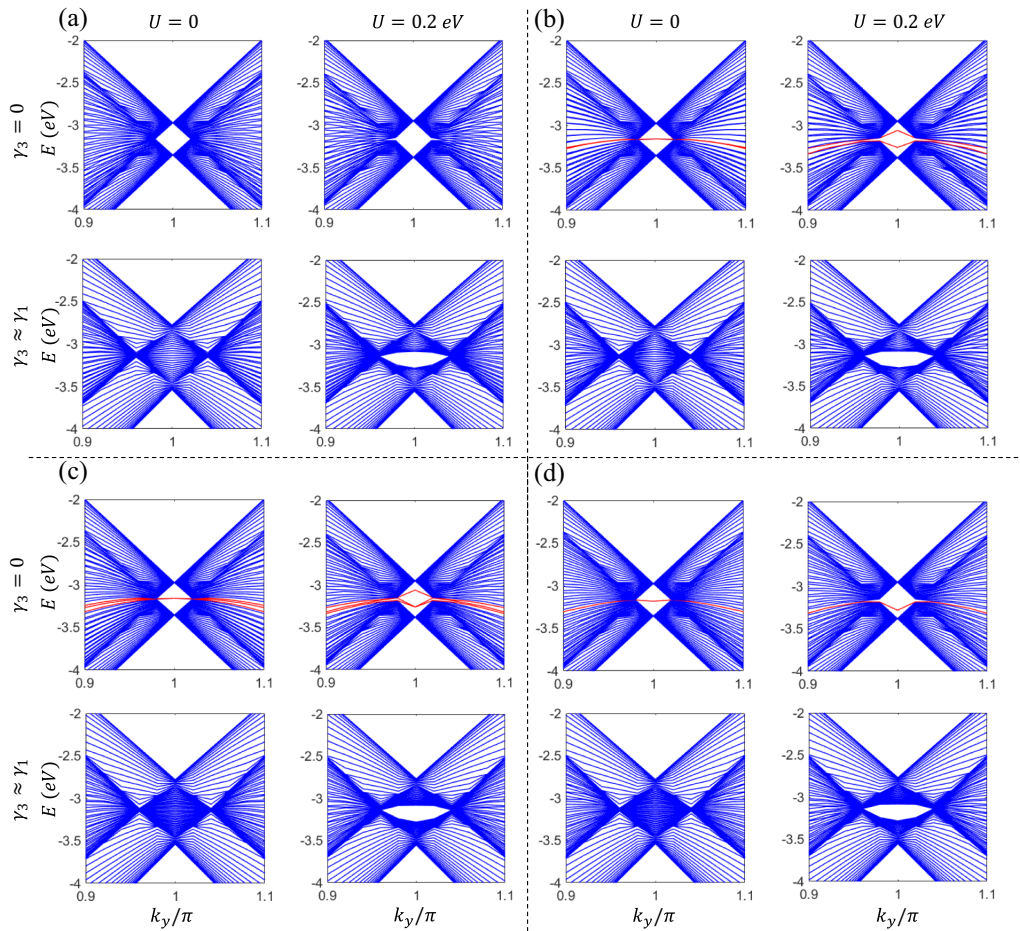


FIG. 9. The band structures in the region marked in Fig. 7, coming from different edge configurations of AB-stacked BLG ribbon with different interlayer bias U and NNN interaction γ_3 . Only the bands with $E < 0$ are shown for simplicity since $E < 0$ and $E > 0$ bands are symmetric. Panels (a)–(d) correspond to the atomic structures shown in Figs. 6(a)–6(d), respectively. The red solid lines show the unexpected edge states appearing in the gap within the bulk bands that are away from zero energy.

the energy of the two-site structure is different from (well separated) that of the bulk four-site structure, their eigenstates would predominantly mix among themselves instead of mix-

ing with states from those four-site structures. Since these two two-sites only exist at the edge, the mixing result would remain edge states. If $\gamma_3 \approx \gamma_1$, two equivalent SSH chains

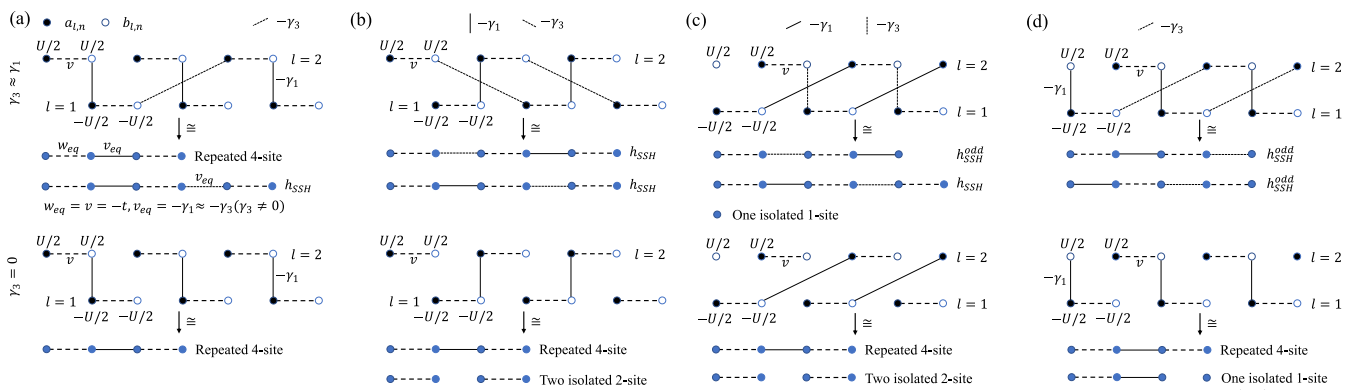


FIG. 10. Effective SSH ladder parametrized by k_y when $k_y \approx \pi$ for different AB-stacked BLG ribbons shown in Figs. 6. Panels (a)–(d) correspond to $H(k_y)$ plotted in in Figs. 6(a)–6(d), respectively. The equivalent lattice structures are shown in blue in each figure, the hopping between sites are given in panel (a).

exist as shown in Fig. 10(b). Each of these chains is the same as the structure of h_{SSH} , leading to no edge states both near the zero energy (Fig. 7) and in the gap within bulk bands [Fig. 9(b)].

The condition is more complicated when we discuss the AB-stacked BLGs with a bearded-zigzag edge. For $H_{\text{ber-zig}}^{\leftarrow}(k_y = \pi)$ with $\gamma_3 = 0$, the same two isolated two-site structures at the end of the chain and repeated decoupled four-site structures appear as in previous cases. Besides, there are also an isolated one-site $h_1 = (U/2)c_1^\dagger c_1$ and a three-site structure at two ends of the chain:

$$h_3 = w_{eq}c_1^\dagger c_2 + v_{eq}c_1^\dagger c_3 + \text{H.c.} - \frac{U}{2}(c_1^\dagger c_1 + c_2^\dagger c_2 - c_3^\dagger c_3), \quad (29)$$

as shown in Fig. 10(c). The two edge states near zero energy are from h_1 and one of eigenstates of h_3 with close-to-zero energy. The three edge states appearing in the gap within bulk bands shown in Fig. 9(c) are naturally described by one eigenstate of h_3 with $E < 0$ and two eigenstates of two $h_2(U = 0)$ with energy $-t$. Again, in the neighborhood of $k_y = \pi$, states from one-, two-, and three-site will mix among themselves instead of mixing with the bulk four-site states due to energy difference. Thus, these states would remain edge states in this neighborhood. When $\gamma_3 \approx \gamma_1$, two SSH chain structures appear with an odd number of sites, each of them provides one edge state near zero energy [57]. All other states of odd-site SSH chains are bulk states. Thus, there are no edge states in the gap within bulk bands, as shown in Fig. 9(c).

At last we discuss $H_{\text{ber-zig}}^{\leftarrow}(k_y = \pi)$. $\gamma_3 = 0$ leads to the repeated decoupled four-site structures, one isolated one-site structure, and one three-site structure, as shown in Fig. 10(d). The edge state shown in Fig. 9(d) comes from one eigenstate of h_3 with $E < 0$. The two near-zero edge states are eigenstate of h_1 and one of eigenstates of h_3 . If $\gamma_3 \approx \gamma_1$, two SSH chains structures appear with odd number of sites. Together they provide two zero-energy edge states, and no edge states in the gap within bulk bands, as shown in Fig. 9(d).

As a conclusion, number of edge states away from Fermi-energy is determined by the number of isolated structures when $k_y = \pi$, which is in turn dependent upon the edge configuration of AB-stacked BLGs.

V. CONCLUSIONS AND DISCUSSIONS

In this paper, we discussed the existence and topology of edge states in AB-stacked BLG ribbon with various edge configurations. We illustrated the correspondence between BLG ribbons and SSH ladders. A detailed topological classification based on a discrete symmetry and topological invariants calculation for an effective 1D bulk Hamiltonian of a SSH ladder $H(k_y, k)$ parametrized by k_y of AB-stacked BLG ribbon was constructed, showing the bulk-edge correspondence between zero-energy edge states of the ribbon and winding number of $H(k_y, k)$.

In addition, we found the existence of bias-induced edge states in the armchair-armchair BLG ribbon. This is not topologically protected, as discussed in the text. However, this is still an interesting result because it implies that edge states can

be produced via a mechanism that does not have anything to do with the edge of systems [58]. We also found a topological phase transition between two topologically nontrivial phases in zigzag-bearded BLG ribbon, corresponding to a twofold degenerate zero-energy edge state existing in the whole k_y region. We demonstrated that, when an edge state crosses the phase transition point, it will switch both layer and edge.

Moreover, we pointed out that some nontopological edge states without the protection of the chiral symmetry can be found in the gap within bulk bands that are away from the zero-energy (Fermi level). The existence and number of these states are sensitive to the edge configurations of BLG ribbons even if their bulk topologies are the same, which can be simply explained by effective Hamiltonians $H(k_y = \pi)$ for different situations. Although we focus only on the honeycomb lattice in this paper, it should be obvious that our study can be generalized to lattices of different shapes, such as Kagome [59–61] and triangular [62] lattices, and of higher dimensions, such as the description of edge states and surface states in three-dimensional topological insulators [63,64]. All of these provide potential directions for further study.

ACKNOWLEDGMENTS

T.X. Tan would like thank Z.A. Hu and F.R. Fan for useful discussions. C. Li would like to thank B. Fu for insightful suggestions. The work is supported by the University Grants Committee/Research Grant Council of the Hong Kong SAR (AoE/P-701/20), the HKU Seed Funding for Strategic Interdisciplinary Research, and the Croucher Senior Research Fellowship.

APPENDIX: THE DIFFERENCE BETWEEN WAVE VECTOR NUMBER k_y AND k

The following example is provided to make the discussion in Sec. II of the main text more concrete. Consider the ribbon depicted in Fig. 1(a); the Hamiltonian is given by Eq. (2) of the text:

$$H_{\text{bea}} = -t \sum_{m=1}^M \left\{ \sum_{n=1}^N [a_{m,n}^\dagger b_{m,n} + b_{m,n}^\dagger (a_{m,n+1} + a_{m+1,n+1})] - b_{m,N}^\dagger (a_{m,1} + a_{m+1,1}) + \text{H.c.} \right\}. \quad (A1)$$

For this specific ribbon, $N = 5$. The value of M is unimportant since the ribbon is infinite (periodic) along that direction. It is a common practice to assume that there is a periodicity in the operator, i.e., $a_{i,j}^{(\dagger)} = a_{i+M,j+N}^{(\dagger)}$ and $b_{i,j}^{(\dagger)} = b_{i+M,j+N}^{(\dagger)}$. Notice that, under this condition, the Hamiltonian given by Eq. (2) is invariant when adding 1 to all the first subscripts of all operators. But it is not invariant when adding 1 to the second subscript of all operators. This difference is due to the term $b_{m,N}^\dagger (a_{m,1} + a_{m+1,1})$, so we say that this term gives the open boundary condition.

By basic solid-state physics, we are allowed to make a Fourier transformation along the invariant direction, which is the direction of the first subscript. The Fourier transformation is given by Eq. (3) of the main text, while the resulting Bloch

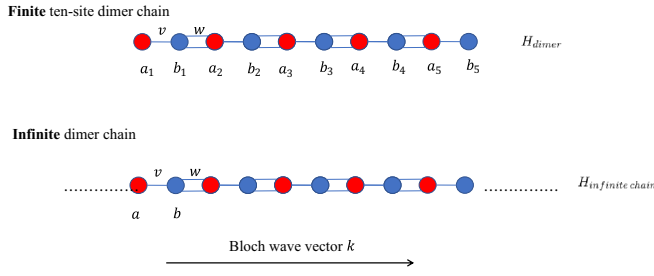


FIG. 11. A schematic illustration of a ten-site SSH chain as well as its bulk. The letters below the circles correspond to operators.

form Hamiltonian is given by Eq. (4). Consider now doing the following redefinition of operators, which is always allowed since it does not affect the band structure:

$$\begin{aligned} a_{k_y, n}^\dagger &\rightarrow a_{k_y, n}^\dagger e^{ik_y n/2}, \\ b_{k_y, n}^\dagger &\rightarrow b_{k_y, n}^\dagger e^{ik_y n/2}. \end{aligned} \quad (\text{A2})$$

After this redefinition, the Hamiltonian in Eq. (4) will be transformed into the form of Eq. (5), which is the following, where a_n (b_n) are shorthand for $a_{k_y, n}$ ($b_{k_y, n}$):

$$H_{\text{bea}}(k_y) = \sum_{n=1}^4 (v a_n^\dagger b_n + w b_n^\dagger a_{n+1}) + v a_N^\dagger b_N + \text{H.c.} \quad (\text{A3})$$

From this point on, we will leave MLG ribbon, and instead consider a ten-site SSH chain as illustrated in Fig. 11. Its intercell coupling w and intracell coupling v are defined as follows:

$$v \equiv -t \quad w \equiv -2t \cos\left(\frac{k_y}{2}\right). \quad (\text{A4})$$

Readers should refrain from associating k_y appearing above with the one obtained in the Fourier transformation of MLG ribbon, but instead should think it just as a parameter on which v and w depend. The Hamiltonian of the ten-site SSH chain is

$$H_{\text{dimer}} = \sum_{n=1}^4 (v a_n^\dagger b_n + w b_n^\dagger a_{n+1}) + v a_N^\dagger b_N + \text{H.c.} \quad (\text{A5})$$

H_{dimer} is formally equivalent to $H_{\text{bea}}(k_y)$, i.e., $H_{\text{dimer}} \cong H_{\text{bea}}(k_y)$. However, it is more obvious that this is an additional trick we can play with this ten-site SSH chain. We can make this chain infinite and obtain a Hamiltonian H_{chain} that can be put in Bloch form, with the corresponding Bloch wave vector k , as used in the main text:

$$\begin{aligned} H_{\text{infinite chain}} &= \sum_{k \in \text{FBZ}} H(k) \\ H(k) &= (v + w e^{-ik}) a_k^\dagger b_k + \text{H.c.} \\ &= \begin{pmatrix} 0 & v + w e^{-ik} \\ v + w e^{ik} & 0 \end{pmatrix}. \end{aligned} \quad (\text{A6})$$

This $H(k)$ is dependent on k_y through v and w . This $H(k)$ is referred to as $h_b(k_y, k)$ in Eq. (6) of the text, with which we can calculate the winding number W for different k_y using Eqs. (7) and (8) of the text. For this specific example, the chiral operator S is

$$S = \begin{pmatrix} 1 & 0 \\ 0 & -1 \end{pmatrix}. \quad (\text{A7})$$

This procedure can be easily generalized to the bilayer case as we use in later sections.

- [1] C. L. Kane and E. J. Mele, Quantum Spin Hall Effect in Graphene, *Phys. Rev. Lett.* **95**, 226801 (2005).
- [2] M. Onoda and N. Nagaosa, Spin Current and Accumulation Generated by the Spin Hall Insulator, *Phys. Rev. Lett.* **95**, 106601 (2005).
- [3] C. Wu, B. A. Bernevig, and S.-C. Zhang, Helical Liquid and the Edge of Quantum Spin Hall Systems, *Phys. Rev. Lett.* **96**, 106401 (2006).
- [4] B. A. Bernevig, T. L. Hughes, and S.-C. Zhang, Quantum spin Hall effect and topological phase transition in HgTe quantum wells, *Science* **314**, 1757 (2006).
- [5] M. Z. Hasan and C. L. Kane, Topological insulators, *Rev. Mod. Phys.* **82**, 3045 (2010).
- [6] G. M. Graf and M. Porta, Bulk-edge correspondence for two-dimensional topological insulators, *Commun. Math. Phys.* **324**, 851 (2013).
- [7] M. S. Rudner, N. H. Lindner, E. Berg, and M. Levin, Anomalous Edge States and the Bulk-Edge Correspondence for Periodically Driven Two-Dimensional Systems, *Phys. Rev. X* **3**, 031005 (2013).
- [8] B. A. Bernevig, *Topological Insulators and Topological Superconductors* (Princeton University Press, 2013).
- [9] J. K. Asbóth, L. Oroszlány, and A. P. Pályi, *A Short Course on Topological Insulators* (Springer International Publishing, Switzerland, 2016).
- [10] C.-K. Chiu, J. C. Y. Teo, A. P. Schnyder, and S. Ryu, Classification of topological quantum matter with symmetries, *Rev. Mod. Phys.* **88**, 035005 (2016).
- [11] G. van Miert, C. Ortix, and C. M. Smith, Topological origin of edge states in two-dimensional inversion-symmetric insulators and semimetals, *2D Mater.* **4**, 015023 (2017).
- [12] R. Saito, G. Dresselhaus, and M. S. Dresselhaus, *Physical Properties of Carbon Nanotubes* (Imperial College Press, London, 1998).
- [13] K. S. Novoselov, A. K. Geims, S. V. Morozov, D. Jiang, Y. Zhang, S. V. Dubonos, I. V. Grigorieva, and A. A. Firsov, Electric field effect in atomically thin carbon films, *Science* **306**, 666 (2004).
- [14] J. C. Meyer, A. K. Geim, M. I. Katsnelson, K. S. Novoselov, T. J. Booth, and S. Roth, The structure of suspended graphene sheets, *Nature (London)* **446**, 60 (2007).
- [15] V. V. Cheianov, V. Fal'ko, and B. L. Altshuler, The focusing of electron flow and a Veselago lens in graphene p-n junctions, *Science* **315**, 1252 (2007).
- [16] B. Uchoa and A. H. Castro Neto, Superconducting States of Pure and Doped Graphene, *Phys. Rev. Lett.* **98**, 146801 (2007).
- [17] B. Huard, J. A. Sulpizio, N. Stander, K. Todd, B. Yang, and D. Goldhaber-Gordon, Transport Measurements Across a Tunable

- Potential Barrier in Graphene, *Phys. Rev. Lett.* **98**, 236803 (2007).
- [18] S. Y. Zhou, G.-H. Gweon, A. V. Fedorov, P. N. First, W. A. de Heer, D.-H. Lee, F. Guinea, A. H. Castro Neto, and A. Lanzara, Substrate-induced bandgap opening in epitaxial graphene, *Nat. Mater.* **6**, 770 (2007).
- [19] A. H. Castro Neto, F. Guinea, N. M. R. Peres, K. S. Novoselov, and A. K. Geim, The electronic properties of graphene, *Rev. Mod. Phys.* **81**, 109 (2009).
- [20] V. Meunier, A. G. Souza Filho, E. B. Barros, and M. S. Dresselhaus, Physical properties of low-dimensional sp^2 -based carbon nanostructures, *Rev. Mod. Phys.* **88**, 025005 (2016).
- [21] P. R. Wallace, The band theory of graphite, *Phys. Rev.* **71**, 622 (1947).
- [22] V. P. Gusynin and S. G. Sharapov, Unconventional Integer Quantum Hall Effect in Graphene, *Phys. Rev. Lett.* **95**, 146801 (2005).
- [23] K. S. Novoselov, A. K. Geim, S. V. Morozov, D. Jiang, M. I. Katsnelson, I. V. Grigorieva, S. V. Dubonos, and A. A. Firsov, Two-dimensional gas of massless Dirac fermions in graphene, *Nature (London)* **438**, 197 (2005).
- [24] Y. B. Zhang, Y.-W. Tan, H. L. Stormer, and P. Kim, Experimental observation of the quantum Hall effect and Berry's phase in graphene, *Nature (London)* **438**, 201 (2005).
- [25] M. I. Katsnelson, K. S. Novoselov, and A. K. Geim, Chiral tunnelling and the Klein paradox in graphene, *Nat. Phys.* **2**, 620 (2006).
- [26] K. S. Novoselov, Z. Jiang, Y. Zhang, S. V. Morozov, H. L. Stormer, U. Zeitler, J. C. Maan, G. S. Boebinger, P. Kim, and A. K. Geim, Room-temperature quantum Hall effect in graphene, *Science* **315**, 1379 (2007).
- [27] D. Xiao, W. Yao, and Q. Niu, Valley-Contrasting Physics in Graphene: Magnetic Moment and Topological Transport, *Phys. Rev. Lett.* **99**, 236809 (2007); W. Yao, D. Xiao, and Q. Niu, Valley-dependent optoelectronics from inversion symmetry breaking, *Phys. Rev. B* **77**, 235406 (2008).
- [28] S. Ryu and Y. Hatsugai, Topological Origin of Zero-Energy Edge States in Particle-Hole Symmetric Systems, *Phys. Rev. Lett.* **89**, 077002 (2002).
- [29] A. Rycerz, J. Tworzydło, and C. W. J. Beenakker, Valley filter and valley valve in graphene, *Nat. Phys.* **3**, 172 (2007).
- [30] W. Yao, S. A. Yang, and Q. Niu, Edge States in Graphene: From Gapped Flat-Band to Gapless Chiral Modes, *Phys. Rev. Lett.* **102**, 096801 (2009).
- [31] P. Delplace, D. Ullmo, and G. Montambaux, Zak phase and the existence of edge states in graphene, *Phys. Rev. B* **84**, 195452 (2011).
- [32] C.-H. Chiu and C.-S. Chu, Effects of edge potential on an armchair-graphene open boundary and nanoribbons, *Phys. Rev. B* **85**, 155444 (2012).
- [33] R. Saito, M. Fujita, G. Dresselhaus, and M. S. Dresselhaus, Electronic structure of graphene tubules based on C_{60} , *Phys. Rev. B* **46**, 1804 (1992).
- [34] C.-A. Li, Pseudo chiral anomaly in zigzag graphene ribbons, *J. Phys.: Condens. Matter* **32**, 025301 (2019).
- [35] S.-L. Zhang and Q. Zhou, Two-leg Su-Schrieffer-Heeger chain with glide reflection symmetry, *Phys. Rev. A* **95**, 061601(R) (2017).
- [36] S. Lieu, Topological symmetry classes for non-Hermitian models and connections to the bosonic Bogoliubov-de Gennes equation, *Phys. Rev. B* **98**, 115135 (2018).
- [37] K. Kawabata, K. Shiozaki, M. Ueda, and M. Sato, Symmetry and Topology in Non-Hermitian Physics, *Phys. Rev. X* **9**, 041015 (2019).
- [38] K. Yokomizo and S. Murakami, Non-Bloch band theory in bosonic Bogoliubov-de Gennes systems, *Phys. Rev. B* **103**, 165123 (2021).
- [39] P. A. Pantaleón and Y. Xian, Effects of edge on-site potential in a honeycomb topological magnon insulator, *J. Phys. Soc. Jpn.* **87**, 064005 (2018).
- [40] S. S. Pershoguba, S. Banerjee, J. C. Lashley, J. Park, H. Ågren, G. Aepli, and A. V. Balatsky, Dirac Magnons in Honeycomb Ferromagnets, *Phys. Rev. X* **8**, 011010 (2018).
- [41] S. Mao, Y. Kuramoto, K.-I. Imura, and A. Yamakage, Analytic theory of edge modes in topological insulators, *J. Phys. Soc. Jpn.* **79**, 124709 (2010).
- [42] Y. Plotnik, M. C. Rechtsman, D. H. Song, M. Heinrich, J. M. Zeuner, S. Nolte, Y. Lumer, N. Malkova, J. J. Xu, A. Szameit, Z. G. Chen, and M. Segev, Observation of unconventional edge states in 'photonic graphene', *Nat. Mater.* **13**, 57 (2014).
- [43] M. Milićević, T. Ozawa, G. Montambaux, I. Carusotto, E. Galopin, A. Lemaître, L. Le Gratiet, I. Sagnes, J. Bloch, and A. Amo, Orbital Edge States in a Photonic Honeycomb Lattice, *Phys. Rev. Lett.* **118**, 107403 (2017).
- [44] K. S. Novoselov, E. McCann, S. V. Morozov, V. I. Fal'ko, M. I. Katsnelson, U. Zeitler, D. Jiang, F. Schedin, and A. K. Geim, Unconventional quantum Hall effect and Berry's phase of 2π in bilayer graphene, *Nat. Phys.* **2**, 177 (2006).
- [45] E. McCann and V. I. Fal'ko, Landau-Level Degeneracy and Quantum Hall Effect in a Graphite Bilayer, *Phys. Rev. Lett.* **96**, 086805 (2006).
- [46] Eduardo V. Castro, N. M. R. Peres, J. M. B. Lopes dos Santos, A. H. Castro Neto, and F. Guinea, Localized States at Zigzag Edges of Bilayer Graphene, *Phys. Rev. Lett.* **100**, 026802 (2008).
- [47] V. Mazo, E. Shimshoni, and H. A. Fertig, Edge states of bilayer graphene in the quantum Hall regime, *Phys. Rev. B* **84**, 045405 (2011).
- [48] R. Sakaguchi and M. Matsumoto, Edge magnon excitation in spin dimer systems, *J. Phys. Soc. Jpn.* **85**, 104707 (2016).
- [49] D. Ghader, Valley-polarized domain wall magnons in 2D ferromagnetic bilayers, *Sci. Rep.* **10**, 16733 (2020); Theoretical realization of rich magnon topology by symmetry-breaking in honeycomb bilayer ferromagnets, *Physica E* **135**, 114984 (2022).
- [50] W.-K. Tse, Z. Qiao, Y. Yao, A. H. MacDonald, and Q. Niu, Quantum anomalous Hall effect in single-layer and bilayer graphene, *Phys. Rev. B* **83**, 155447 (2011).
- [51] W. Li and R. Tao, Edge states of monolayer and bilayer graphene nanoribbons, *J. Phys. Soc. Jpn.* **81**, 024704 (2012).
- [52] A. B. Kuzmenko, I. Crassee, D. van der Marel, P. Blake, and K. S. Novoselov, Determination of the gate-tunable band gap and tight-binding parameters in bilayer graphene using infrared spectroscopy, *Phys. Rev. B* **80**, 165406 (2009).
- [53] E. McCann and M. Koshino, The electronic properties of bilayer graphene, *Rep. Prog. Phys.* **76**, 056503 (2013).

- [54] J. L. Mañes, F. Guinea, and M. A. H. Vozmediano, Existence and topological stability of Fermi points in multilayered graphene, *Phys. Rev. B* **75**, 155424 (2007).
- [55] L. Lin, Y. Ke, and C. Lee, Real-space representation of the winding number for a one-dimensional chiral-symmetric topological insulator, *Phys. Rev. B* **103**, 224208 (2021).
- [56] T. Kato, *Perturbation Theory for Linear Operators* (Springer Science and Business Media, 2013).
- [57] H.-T. Chen, C.-H. Chang, and Hsien-chung Kao, Connection between the winding number and the Chern number, *Chin. J. Phys.* **72**, 50 (2021).
- [58] The presence of these edge states is still dependent on edge configuration, since only one of the two edge configurations of BLG arm-arm ribbon show them. However, the mechanism itself, i.e. bias, does not treat the atoms on the edge differently from those deep inside the bulk. This is different from edge states induced by modulating only the edge onsite energy. More specifically, after we impose this bias, the effective k_y -parametrized SSH ladder for BLG arm-arm ribbon still has a bulk Hamiltonian, on which we can discuss the topology. However, if we only modulate the onsite energy on the edge of BLG arm-arm ribbon, the effective SSH ladder does not have a bulk Hamiltonian.
- [59] T.-H. Han, J. S. Helton, S. Chu, D. G. Nocera, J. A. Rodriguez-Rivera, C. Broholm, and Y. S. Lee, Fractionalized excitations in the spin-liquid state of a kagome-lattice antiferromagnet, *Nature (London)* **492**, 406 (2012).
- [60] X. Ni, M. A. Gorlach, A. Alu, and A. B. Khanikaev, Topological edge states in acoustic kagome lattices, *New J. Phys.* **19**, 055002 (2017).
- [61] N. J. Ghimire and I. I. Mazin, Topology and correlations on the kagome lattice, *Nat. Mater.* **19**, 137 (2020).
- [62] T. Kurumaji, T. Nakajima, M. Hirschberger, A. Kikkawa, Y. Yamasaki, H. Sagayama, H. Nakao, Y. Taguchi, T. Arima, and Y. Tokura, Skyrmion lattice with a giant topological Hall effect in a frustrated triangular-lattice magnet, *Science* **30**, 914 (2019).
- [63] J. C. Y. Teo, L. Fu, and C. L. Kane, Surface states and topological invariants in three-dimensional topological insulators: Application to $\text{Bi}_{1-x}\text{Sb}_x$, *Phys. Rev. B* **78**, 045426 (2008).
- [64] W.-Y. Shan, H.-Z. Lu, and S.-Q. Shen, Effective continuous model for surface states and thin films of three-dimensional topological insulators, *New J. Phys.* **12**, 043048 (2010).